Department of Engineering Physics and Mathematics
Helsinki University of Technology
FIN-02015 HUT, Finland

NUMERICAL CALCULATIONS ON VORTEX PHENOMENA IN HELIUM SUPERFLUIDS

Juha Kopu

Low Temperature Laboratory

Dissertation for the degree of Doctor of Science in Technology to be presented
with due permission of the Department of Engineering Physics and Mathematics
for public examination and debate in Auditorium F1 at Helsinki University of
Technology (Espoo, Finland) on the 9th of June, 2001, at 12 o'clock noon.

Espoo 2001

Keywords: superfluid, vortices, textures, critical velocity, NMR

Abstract

This thesis reports numerical calculations on quantized vortices in ^{4}He and ^{3}He superfluids. Vortices are of crucial importance in understanding many of the superfluid properties. All the calculations presented in the thesis have experimental relevance, either in understanding measured results or in predicting the outcome of planned experiments.

Superfluid ^{4}He has been observed to exhibit incomplete wetting on certain solid substrates. The variations in the thickness of the fluid layer are explained by a model with a nonuniform distribution of pinned vortices.

Superfluid ^{3}He under weak perturbations (due to container walls, flow and magnetic fields) is studied with the hydrostatic theory. Within this theory, the equilibrium properties of the superfluid are controlled by the distribution, *i.e.* the texture, of the order parameter describing the superfluid state.

In the anisotropic A phase of ^{3}He, vorticity usually appears in doubly-quantized continuous vortices, having no singular core. They can be created by applying a flow with a velocity exceeding an experimentally measurable threshold. The critical velocity can be theoretically identified with the instability of the underlying order-parameter distribution. The flow textures and critical velocities in ^{3}He-A are calculated for different initial configurations in both one-dimensional and two-dimensional geometries.

The full transverse NMR spectrum of ^{3}He-B in a cylindrical container is calculated numerically. The effects of rotation, magnetic field and the number of vortices are included in the model. The results are used to determine the optimal sensitivity for observing changes in the number of vortices, the finite-size effect due to the end plates of the cylinder, and the change of absorption induced by the presence of a spin-mass vortex.

ISBN 951-22-5488-3

Contents

1 Introduction

This thesis presents theoretical studies on superfluidity, a property exhibited by the two stable isotopes, ^{4}He and ^{3}He, of liquid helium at low temperatures. In many cases, existing theories explain successfully experimental results on superfluid systems. However, realistic models, even in the simplest cases, usually lead to mathematical problems either difficult or impossible to solve with analytical methods. Numerical computation is often needed to achieve quantitative agreement between theory and measurements.

The main characteristic feature of superfluids is the ability to flow without friction, which is one of the few known manifestations of quantum-mechanical behaviour on a large scale. The dissipationless supercurrent is caused by a large number of particles moving in a coherent fashion, like a single macroscopic entity. Such a flow can be generated experimentally *e.g.* by driving a piston through a channel containing superfluid helium, or by placing the superfluid in a rotating container. However, the frictionless flow can only be sustained when its velocity is sufficiently low. If the velocity exceeds a critical value, dissipation sets in through the appearance of quantized vortices, linear objects surrounded by stable circulating flow. Vortices are of crucial importance in understanding various properties of superfluids.

My thesis presents numerical calculations on vortex-related phenomena in three different superfluid systems: superfluid ^{4}He (^{4}He-II) and the A and B phases of ^{3}He. Section 1 introduces the most important theoretical concepts relevant to the specific research projects described in the subsequent sections.

The thickness of the ^{4}He-II film covering a rough solid substrate is affected by the presence of vortices trapped by surface imperfections (see Fig. 1a). In Sec. 2, I describe numerical calculations on the equilibrium film profile of ^{4}He-II in a situation with an inhomogeneous distribution of trapped vortices [P1]. The calculations suggest the existence of transition regions where the film thickness varies rapidly, reminiscent of three-phase contact angles.

The superfluid state in ^{3}He has a nontrivial internal structure. The associated degrees of freedom can be formally represented by unit-vector fields, one ($\hat{\mathbf{n}}$) in ^{3}He-B and two ($\hat{\mathbf{l}}$ and $\hat{\mathbf{d}}$) in ^{3}He-A, defined in the volume of the liquid. Different internal and external influences tend to orient these fields, causing the formation of textures, weakly inhomogeneous spatial distributions of the vector fields.

In Sec. 3, I describe calculations on vortex formation in the A phase of ^{3}He. The formation of vortices in ^{3}He-A is connected to a flow-induced textural transition. I have

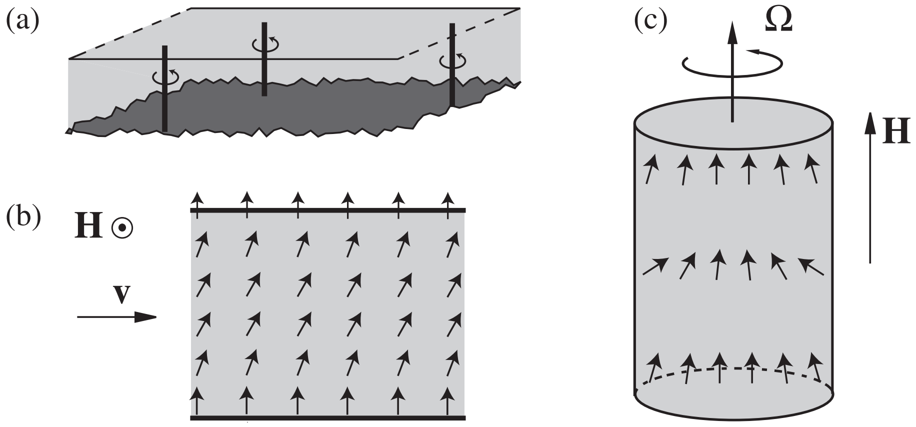

Figure 1: (a) Vortex lines pinned by surface irregularities in a ^{4}He-II film. (b) The $\hat{\mathbf{l}}$ field of ^{3}He-A for channel flow of velocity $\mathbf{v}$ in the presence of a magnetic field $\mathbf{H}$. (c) The $\hat{\mathbf{n}}$ field of ^{3}He-B in a cylinder rotating with angular velocity Ω in the presence of an axial magnetic field.

determined the associated critical velocity by calculating the equilibrium texture in a channel (see Fig. 1b) as a function of the driving velocity [P2–P4]. I have performed detailed studies on various different initial states using both one-dimensional and two-dimensional models.

In the B phase, the presence of vortices in a rotating cylindrical container induces modifications to the overall texture (Fig. 1c). This can be observed experimentally using methods based on nuclear magnetic resonance (NMR). In Sec. 4, I present calculations on the NMR response of ^{3}He-B as a function of the number of vortex lines and several other external parameters [P5], and in the presence of a spin-mass vortex [P6].

All the calculations are related to measurements, and in most cases quantitative agreement with experiments is achieved without adjustable parameters.

1.1 Order parameter

The properties of superfluids arise from the macroscopic occupation of a single quantum-mechanical state below a critical temperature ($T_\lambda \approx 2$ K for ^{4}He, $T_\mathrm{c} \approx 3$ mK for ^{3}He). The low-temperature phase can be described by introducing an order parameter that reflects the broken symmetries associated with the phase transition. In the case of ^{4}He-II, the order parameter has the form of a scalar wave function [1]

$$\psi = |\psi| e^{i\Phi} \tag{1}$$

of the macroscopically occupied quantum state. The wave function describes the coherent state of structureless ^{4}He atoms with zero spin, $S = 0$, and zero internal orbital angular momentum, $L = 0$. The magnitude $|\psi|$ of the order parameter has a fixed value, determined by the condensation energy of the superfluid (the energy gained in the process of forming the coherent state). The phase Φ, however, is arbitrary and different choices represent energetically degenerate equilibrium states. Such quantities are sometimes referred to as soft variables or degeneracy parameters. More important than the actual value of Φ is the concept of rigidity, *i.e.* a spatial change in Φ involves a cost of energy. The balance between this gradient energy and the condensation energy defines a characteristic length of a superfluid, the coherence length ξ, which in ^{4}He-II is of the order of 0.1 nm.

In ^{3}He, the superfluid condensate is formed by correlated particle pairs, Cooper pairs, which are in the same two-particle state having a nonzero spin $S = 1$ and a relative orbital angular momentum $L = 1$ [2–4]. Due to the weakness of the pairing interaction, the condensation energy is very small, and superfluidity is only observed at millikelvin temperatures. Also, the coherence length in ^{3}He is larger than in ^{4}He-II: $\xi \sim 70 - 100$ nm. The Cooper-pair state is determined by nine complex amplitudes, corresponding to the three possible projections of both S_z and L_z. The order parameter for superfluid ^{3}He is usually represented by a complex 3×3 matrix $A_{\mu j}$, where the index μ refers to spin and j to orbital degrees of freedom. Like ^{4}He-II, superfluid ^{3}He shows anomalous flow properties. Owing to the complicated order-parameter structure, superfluid ^{3}He also exhibits magnetic and liquid-crystal-like behaviour, supports many kinds of topological defects, including a variety of vortices, and can exist in several superfluid phases with different symmetry properties [5–8].

The stable superfluid phases observed in nature correspond to certain special forms of the general 3×3 matrix. At low pressures, the equilibrium structure is called the B phase, and the corresponding (unperturbed) order parameter has the form

$$A_{\mu j} \propto e^{i\Phi} R_{\mu j}, \tag{2}$$

where $R_{\mu j}$ is a three-dimensional rotation matrix. Apart from the phase Φ, the order parameter is degenerate also with respect to the structure of the rotation matrix, which can conveniently be parametrized by the axis $\hat{\mathbf{n}}$ (of unit length) and the angle θ of the rotation.

At pressures above 21 bar, the superfluid transition leads to a different state, the A phase. The order parameter for this phase can be written

$$A_{\mu j} \propto \hat{d}_\mu (\hat{m}_j + i\hat{n}_j), \tag{3}$$

where the spin part is determined by a unit vector $\hat{\mathbf{d}}$ and the orbital part by two mutually orthogonal unit vectors $\hat{\mathbf{m}}$ and $\hat{\mathbf{n}}$. It is customary to define a third unit vector $\hat{\mathbf{l}} = \hat{\mathbf{m}} \times \hat{\mathbf{n}}$ so that $\{\hat{\mathbf{m}}, \hat{\mathbf{n}}, \hat{\mathbf{l}}\}$ form an orthonormal triad in the orbital space. No explicit phase factor appears in Eq. (3). Instead, the phase information is contained in the orientation of the orbital triad: rotating $\hat{\mathbf{m}}$ and $\hat{\mathbf{n}}$ by an angle $-\Phi$ around $\hat{\mathbf{l}}$ is equivalent to multiplying the order parameter by $\exp(i\Phi)$. The vector $\hat{\mathbf{l}}$ gives the direction of the angular momentum of the Cooper pair, and $\hat{\mathbf{d}}$ is perpendicular to the spin of the pair. In contrast to ^{4}He-II and also largely to ^{3}He-B, the existence of preferred directions in spin and orbital spaces in the A phase results in strong anisotropy.

1.2 Vorticity in superfluids

Many properties of superfluid systems can be explained with the phenomenological two-fluid model, in which the superfluid is regarded as a mixture of two liquids [1]. One of them is a normal viscous liquid with density ρ_n and velocity $\mathbf{v}_\mathrm{n}$, and the other is superfluid, with density $\rho_\mathrm{s} = \rho - \rho_\mathrm{n}$ (ρ is the total density) and velocity $\mathbf{v}_\mathrm{s}$. The behaviour of the superfluid component is described by the order parameter. In particular, the superfluid velocity $\mathbf{v}_\mathrm{s}$ of the nondissipative flow in ^{4}He-II appears as a result of the existence of a macroscopic phase variable. It is given by the spatial gradient of the phase,

$$\mathbf{v}_\mathrm{s} = \frac{\hbar}{m_4} \nabla \Phi, \tag{4}$$

where m_4 is the mass of the ^{4}He atom. The form of the velocity implies that the superfluid flow in ^{4}He-II is potential, *i.e.* satisfies the condition $\nabla \times \mathbf{v}_\mathrm{s} = 0$. Still, this does not rule out the possibility of rotational motion being described by Eq. (4). This can be seen by investigating the circulation κ, *i.e.* the line integral of $\mathbf{v}_\mathrm{s}$, along a closed contour in ^{4}He-II. Since the single-valued phase Φ can only change by a multiple of 2π on the closed curve, it follows that

$$\kappa = \oint d\mathbf{r} \cdot \mathbf{v}_\mathrm{s} = \frac{\hbar}{m_4} \oint d\mathbf{r} \cdot \nabla \Phi = \frac{\hbar}{m_4}(2\pi n) = n\frac{h}{m_4}, \tag{5}$$

where n is an integer. Therefore, the circulation in ^{4}He-II is quantized to integral multiples of h/m_4. In a simply connected container, a nonzero value of n implies the presence of one or more singular regions inside the contour of integration, inside which the order parameter given by Eq. (1) vanishes. These regions form the cores of vortex lines [9]. Because the order parameter inside the core differs from that in bulk superfluid, the size of the core is determined by the coherence length ξ. In equilibrium situations, each vortex line carries one quantum of circulation.

Because of the similar phase factor in the order parameter, the above discussion of ^{4}He-II also applies to ^{3}He-B with a few modifications. Since the condensate is formed by pairs of atoms (with mass m_3), the superfluid velocity is given by

$$\mathbf{v}_\mathrm{s} = \frac{\hbar}{2m_3}\nabla\Phi, \tag{6}$$

and the circulation quantum is $\kappa_0 = h/(2m_3)$. The size of the vortex cores is larger because of the longer coherence length. Moreover, due to the additional degrees of freedom, the order parameter remains nonzero also inside the core (although some of the components vanish). In fact, two different core structures have been observed experimentally in the B phase [10], with different order-parameter distributions and symmetries [11, 12]. In addition to these two, a third kind of vortex has been observed in ^{3}He-B: a spin-mass vortex with spin currents as well as mass currents circulating around its core [13].

The anisotropic ^{3}He-A differs noticeably from the previous two superfluids. The expression for the superfluid velocity in the A phase is

$$\mathbf{v}_\mathrm{s} = \frac{\hbar}{2m_3}\sum_j \hat{m}_j\nabla\hat{n}_j. \tag{7}$$

The important consequence of Eq. (7) is that the curl of $\mathbf{v}_\mathrm{s}$ can be nonzero, depending on the spatial variation of the orbital triad [14]. Therefore, the circulation in the A phase can in principle have any value. However, order-parameter variations require energy, which restricts the formation of spatial gradients. For example, if $\hat{\mathbf{l}}$ is constant or constrained to vary in a plane, the superfluid velocity becomes potential. It turns out that not only is quantized vorticity present in ^{3}He-A, but it can also appear in many different forms [15]. In addition to the singular vortices that have a strongly distorted core structure and carry one quantum of circulation (like the vortices in ^{4}He-II and ^{3}He-B), three different kinds of doubly-quantized continuous vortices have been identified in the A phase. In the core of a continuous vortex, the bulk state of Eq. (3) is retained everywhere, and the circulation arises from the spatial variation of the $\hat{\mathbf{l}}$ vector. Furthermore, vorticity in ^{3}He-A can reside on a planar structure, called a vortex sheet.

1.3 Textures in ^{3}He

The equilibrium properties of superfluid ^{3}He can be determined by the hydrostatic theory. The theory is applicable in situations where the external perturbations are weak enough not to distort the order-parameter structure from the bulk form, but merely affect the orientation of the soft degrees of freedom (in other words, the length scales associated with the perturbations are much larger than the coherence length ξ). The possible influences include *e.g.* magnetic fields, the walls of the container, and externally applied flow. The circumstances where several influences compete with each other can result in the formation of a nonuniform distribution of the degeneracy variables, which is called a texture. The following discussion introduces the main orienting interactions with their respective free-energy contributions in both B and A phases.

In ^{3}He-B, the textures of the order parameter (2) arise from the spatial variations of the rotation matrix $\overset{\leftrightarrow}{R}(\hat{\mathbf{n}}, \theta)$. The most important interaction that affects the structure of $\overset{\leftrightarrow}{R}$ is the dipole interaction between the nuclear moments of the ^{3}He atoms. It is not sensitive to the direction of $\hat{\mathbf{n}}$, but it lifts the degeneracy in the rotation angle by favouring $\theta \approx 104°$ over distances larger than the characteristic length of the interaction, the dipole length $\xi_\mathrm{D} \sim 10\mu$m. The texture problem is thus reduced to finding the distribution $\hat{\mathbf{n}}(\mathbf{r})$ [16]. A large multitude of external influences tend to orient $\hat{\mathbf{n}}$ [17]. In our calculations, we take into account only the leading ones in the presence of a large magnetic field.

An external magnetic field $\mathbf{H}$ induces a small orientational effect on $\hat{\mathbf{n}}$ through the dipole coupling, with an energy [16]

$$F_\mathrm{DH} = -a \int d^3\mathbf{r}\, (\hat{\mathbf{n}} \cdot \mathbf{H})^2, \tag{8}$$

where the integration is performed over the volume of the sample. A magnetic field thus tends to have $\hat{\mathbf{n}} \parallel \mathbf{H}$. If a counterflow, *i.e.* a difference $\mathbf{v}_\mathrm{n} - \mathbf{v}_\mathrm{s}$ between the velocities of the normal and superfluid components, is set up in the system, the associated flow energy has the form [18]

$$F_\mathrm{HV} = -\lambda_\mathrm{HV} \int d^3\mathbf{r}\, [\mathbf{H} \cdot \overset{\leftrightarrow}{R} \cdot (\mathbf{v}_\mathrm{n} - \mathbf{v}_\mathrm{s})]^2. \tag{9}$$

It is customary to define the dipole velocity $v_\mathrm{D} = \sqrt{2a/(5\lambda_\mathrm{HV})} \sim 1$ mm/s. Because of the order-parameter rigidity, all spatial variations are associated with a gradient energy [16,17]

$$F_\mathrm{G} = \int d^3\mathbf{r} \left[\lambda_\mathrm{G1} \frac{\partial R_{\alpha i}}{\partial r_i} \frac{\partial R_{\alpha j}}{\partial r_j} + \lambda_\mathrm{G2} \frac{\partial R_{\alpha j}}{\partial r_i} \frac{\partial R_{\alpha j}}{\partial r_i} \right], \tag{10}$$

which together with $F_{\rm DH}$ determines the length scale of the texture, the magnetic coherence length $\xi_{\rm H} = \sqrt{65\lambda_{\rm G2}/(8aH^2)} \sim 1$ mm. In addition to the bulk energies (8)–(10), the walls of the container induce a boundary interaction [16]

$$F_{\rm SH} = -d \int d^2\mathbf{r}\, (\mathbf{H} \cdot \overleftrightarrow{R} \cdot \hat{\mathbf{s}})^2, \tag{11}$$

where the integration is over the surface of the wall, the normal of which (pointing towards the superfluid) is given by the unit vector $\hat{\mathbf{s}}$. Another boundary energy arises from equilibrium spin currents at the surface [19],

$$F_{\rm SG} = \lambda_{\rm SG} \int d^2\mathbf{r}\ \hat{s}_j R_{\alpha j} \frac{\partial R_{\alpha i}}{\partial r_i}. \tag{12}$$

This energy term also includes a surface contribution from the gradient energy [16]. The last orienting interaction arises from the distortion of the bulk state inside the vortex cores [20]. If the orientation of the vortex line is given by the unit vector $\hat{\mathbf{l}}_{\rm V}$, the associated free energy of the interaction is

$$F_{\rm LH} = \lambda_{\rm LH} \int_{\rm L} d^3\mathbf{r}\, (\mathbf{H} \cdot \overleftrightarrow{R} \cdot \hat{\mathbf{l}}_{\rm V})^2, \tag{13}$$

where the integral is to be calculated over the region occupied by the vortices. Finally, the equilibrium order-parameter texture in ^{3}He-B is determined by minimizing the sum of the individual free-energy contributions in Eqs. (8)–(13).

In superfluid ^{3}He-A, the free energy is customarily expressed in terms of the vector fields $\hat{\mathbf{d}}$ and $\hat{\mathbf{l}}$, and the superfluid velocity $\mathbf{v}_{\rm s}$ [3]. The dipole interaction in the A phase tends to align the anisotropy axes $\hat{\mathbf{d}}$ and $\hat{\mathbf{l}}$ parallel to each other. The corresponding free-energy density is of the form

$$f_{\rm d} = -\tfrac{1}{2}\lambda_{\rm d}(\hat{\mathbf{d}} \cdot \hat{\mathbf{l}})^2. \tag{14}$$

Because the Cooper-pair spin is perpendicular to $\hat{\mathbf{d}}$, an external magnetic field prefers the orientation $\hat{\mathbf{d}} \perp \mathbf{H}$, with the energy density

$$f_{\rm h} = \tfrac{1}{2}\lambda_{\rm h}(\hat{\mathbf{d}} \cdot \mathbf{H})^2. \tag{15}$$

With Eqs. (14) and (15) it is possible to define a characteristic magnetic-field strength, the dipole field $H_{\rm d}$, according to $H_{\rm d} = \sqrt{\lambda_{\rm d}/\lambda_{\rm h}}$. Consequently, if $H \gg H_{\rm d} \sim 2$ mT, the vector $\hat{\mathbf{d}}$ is constrained to lie in a plane perpendicular to $\mathbf{H}$. The gradient energy corresponding to spatial variations in the order parameter can be written as

$$\begin{aligned} f_{\mathrm{gr}} &= \tfrac{1}{2}\rho_\perp \mathbf{v}_{\mathrm{s}}^2 + \tfrac{1}{2}(\rho_\parallel - \rho_\perp)(\hat{\mathbf{l}}\cdot\mathbf{v}_{\mathrm{s}})^2 \\ &+ C\mathbf{v}_{\mathrm{s}}\cdot\nabla\times\hat{\mathbf{l}} - C_0(\hat{\mathbf{l}}\cdot\mathbf{v}_{\mathrm{s}})(\hat{\mathbf{l}}\cdot\nabla\times\hat{\mathbf{l}}) \\ &+ \tfrac{1}{2}K_{\mathrm{s}}(\nabla\cdot\hat{\mathbf{l}})^2 + \tfrac{1}{2}K_{\mathrm{t}}(\hat{\mathbf{l}}\cdot\nabla\times\hat{\mathbf{l}})^2 + \tfrac{1}{2}K_{\mathrm{b}}|\hat{\mathbf{l}}\times(\nabla\times\hat{\mathbf{l}})|^2 \\ &+ \tfrac{1}{2}K_5|(\hat{\mathbf{l}}\cdot\nabla)\hat{\mathbf{d}}|^2 + \tfrac{1}{2}K_6[(\hat{\mathbf{l}}\times\nabla)_i\hat{\mathbf{d}}_j)]^2. \end{aligned} \tag{16}$$

The first two terms on the right-hand side of Eq. (16) describe the kinetic energy in the anisotropic A phase; the quantities $\rho_\parallel$ and $\rho_\perp$ are the components of the superfluid-density tensor in the directions parallel and perpendicular to $\hat{\mathbf{l}}$, respectively. The next two terms arise because of the coupling between the superfluid velocity and an inhomogeneous $\hat{\mathbf{l}}$ texture. The five remaining terms are the energies due to bending of $\hat{\mathbf{l}}$ and $\hat{\mathbf{d}}$. The characteristic velocity in the hydrostatics of ^{3}He-A is the dipole velocity $v_{\mathrm{d}} = \sqrt{\lambda_{\mathrm{d}}/\rho_\parallel}$, and the length scale of the textures is the dipole coherence length $\xi_{\mathrm{d}} = [\hbar/(2m_3)]\sqrt{\rho_\parallel/\lambda_{\mathrm{d}}} \sim 10\ \mu$m.

In addition to the bulk energies (14)–(16), solid boundaries exert a strong influence on the orbital part of the order parameter. As a result, $\hat{\mathbf{l}}$ is fixed perpendicular to the walls of the container. Together with this boundary condition, the equilibrium order-parameter structure in the A phase is determined by minimizing the total free energy

$$F = \int d^3\mathbf{r}\,(f_{\mathrm{d}} + f_{\mathrm{h}} + f_{\mathrm{gr}}). \tag{17}$$

The numerical values as functions of external conditions (temperature, pressure, etc.) of the various prefactors in the interaction energies in Eqs. (8)–(16) can be obtained by using a more fundamental theory, the quasiclassical theory of ^{3}He [21]. This process is too involved to be discussed here; for details, see Refs. [17] (B phase) and [22] (A phase).

1.4 Superfluids in rotation

One of the most effective methods of creating quantized vortices and studying their properties is to rotate a cylindrical container of superfluid around its axis. At a constant angular velocity of rotation $\boldsymbol{\Omega}$, the viscous normal component of the superfluid rotates like a solid body, *i.e.*

$$\mathbf{v}_{\mathrm{n}} = \boldsymbol{\Omega}\times\mathbf{r}, \tag{18}$$

which implies a nonzero vorticity, $\nabla\times\mathbf{v}_{\mathrm{n}} = 2\boldsymbol{\Omega}$ (the position vector $\mathbf{r}$ is measured from the cylinder axis). For a potential superfluid-velocity field, $\nabla\times\mathbf{v}_{\mathrm{s}} = 0$, the solid-body

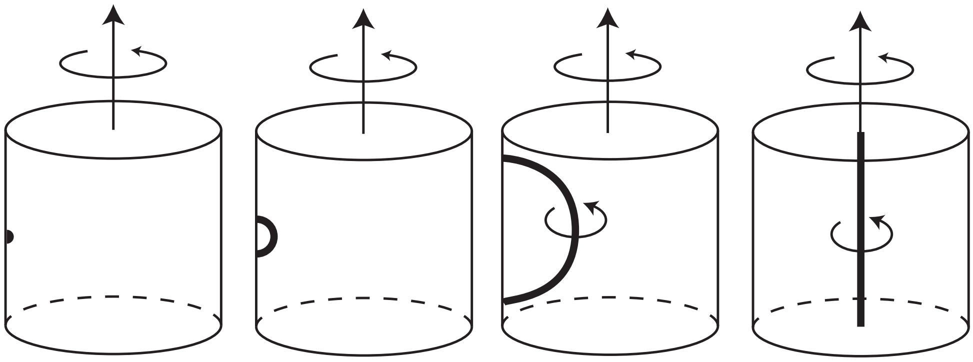

Figure 2: The process of vortex creation in a rotating superfluid (schematic). If the angular velocity is sufficiently high, an initially small vortex loop expands under the influence of counterflow and, finally, comes to rest at the cylinder axis as a rectilinear vortex line.

rotation is forbidden. Thus the superfluid component remains stationary at small Ω. On increasing Ω, however, this state becomes unstable towards having vortex lines in the cylinder. The appearance of vortices reduces the counterflow $\mathbf{v}_\mathrm{n} - \mathbf{v}_\mathrm{s}$ and the kinetic energy of the rotating liquid (see Fig. 2).

At present, the structure and properties of equilibrium vortex states in ^{4}He-II are already well established [9]. At a given angular velocity Ω, a cylindrical container of ^{4}He-II is threaded by rectilinear vortex lines that are parallel to the cylinder axis, and distributed in a regular array with an areal density of

$$n_\mathrm{v} = \frac{2\Omega}{\kappa}. \tag{19}$$

This equation follows from the condition that the circulations of the superfluid-velocity and normal-velocity fields are equal. On accelerating (decelerating) the rotation velocity, vortex nucleation (annihilation) takes place at the container walls, to maintain the equilibrium distribution of Eq. (19). Roughly similar behaviour is also exhibited by ^{3}He superfluids, but a number of differences can be observed in the details.

The critical angular velocities Ω_c for the appearance of vortices in ^{4}He-II are extremely low. In fact, it is practically impossible to achieve a vortex-free state in ^{4}He-II in a rotating cylinder. The critical velocities are believed to reflect the unpinning of pre-existing vortices (formed during the cooldown) from the container walls. They are also very difficult to measure, because thermal fluctuations and quantum tunnelling reduce the nucleation threshold. However, neither of these mechanisms affects the process of vortex creation in superfluid ^{3}He because of the lower temperatures and the longer coherence length ξ. Therefore, the critical velocities in ^{3}He-B and ^{3}He-A describe intrinsic instabilities of the superfluid state.

In the B phase, the disruption of the initial bulk state necessary to produce vortices with a singular core involves a large energy barrier to be overcome by the counterflow. Even though the surface roughness of the walls can reduce the critical velocities considerably, they are still high, typically of the order of several mm/s. Therefore, ^{3}He-B is able to support metastable rotating states, where the number of vortices differs from that given by Eq. (19). In these cases, the vortices are situated in a central cluster at the cylinder axis, forming a vortex bundle.

In ^{3}He-A, the critical velocities are low because a suppression of the bulk order parameter (3) is not necessary for the creation of continuous vortices; an inhomogeneous orbital texture is sufficient. Even the surface roughness does not play a role in the nucleation process because of the boundary condition on the $\hat{\mathbf{l}}$ vector that restricts the vortex formation to take place at a minimum distance of $\sim \xi_\mathrm{d}$ from the wall. Therefore, with ^{3}He-A, it is possible to study the intrinsic stability of superflow under exceptionally ideal conditions.

1.5 NMR in ^{3}He

A successful method of extracting information on the order-parameter distributions in the superfluid phases of ^{3}He is provided by nuclear magnetic resonance. The NMR techniques discussed in this thesis study the linear response of the superfluid subjected to a static magnetic field $\mathbf{H} \parallel \hat{\mathbf{z}}$ and a weak radio-frequency field $\mathbf{H}_\mathrm{rf} \perp \mathbf{H}$ ($H_\mathrm{rf} \ll H$). In the normal state, resonance absorption occurs at the Larmor frequency $\omega_0 = \gamma H$, where γ is the gyromagnetic ratio of the ^{3}He nucleus. In the superfluid state, the NMR response is determined by the coupled dynamical equations for the spin density and the spin part of the order parameter [23].

In the B phase, the frequency ω of the transverse resonance depends on the relative orientation of the static field $\mathbf{H}$ and the vector $\hat{\mathbf{n}}$. By taking $\mathbf{H} \parallel \hat{\mathbf{z}}$ and expressing $\hat{\mathbf{n}} = (-\hat{\mathbf{r}} \cos\alpha + \hat{\boldsymbol{\phi}} \sin\alpha) \sin\beta + \hat{\mathbf{z}} \cos\beta$ in cylindrical coordinates, the resonance frequency can be written in the high-field limit in the approximate form

$$\omega = \sqrt{\omega_0^2 + \Omega_\mathrm{B}^2 \sin^2\beta} \approx \omega_0 + \frac{\Omega_\mathrm{B}^2}{2\omega_0} \sin^2\beta, \tag{20}$$

where Ω_B is the B-phase longitudinal resonance frequency. Therefore, if $\hat{\mathbf{n}}$ is not parallel to $\mathbf{H}$, the resonance frequency is shifted above the Larmor value. The overall spectrum can be obtained by the local oscillator model, *i.e.* by considering the fluid as an assembly of uncoupled oscillators with frequencies determined by the local value of $\beta(\mathbf{r})$ according to (20). The NMR line shape is given by the distribution of the individual contributions,

$$f(\omega) = \frac{1}{V}\int d^3\mathbf{r}\,\delta[\omega - \omega(\mathbf{r})], \tag{21}$$

where V is the volume of the sample. It follows that whenever $\omega(\mathbf{r})$, or equivalently $\beta(\mathbf{r})$, has a constant value over a larger region, the absorption spectrum has a peak at this frequency.

In ^{3}He-A, the static field $\mathbf{H}$ confines the unperturbed $\hat{\mathbf{d}}_0 = \hat{\mathbf{x}}\cos\theta_0 + \hat{\mathbf{y}}\sin\theta_0$ to the plane perpendicular to it. In the presence of a weak oscillating field, $\hat{\mathbf{d}}$ acquires a small component, $\hat{d}_z(\mathbf{r}) = \psi(\mathbf{r})$, along $\mathbf{H}$. This component satisfies a Schrödinger-like equation [24]

$$-[\tilde{K}_6\nabla^2 + (\tilde{K}_5 - \tilde{K}_6)\nabla\cdot\hat{\mathbf{l}}\hat{\mathbf{l}}\cdot\nabla]\psi + U\psi = (R_\perp^2 - 1)\psi, \tag{22}$$

where $\tilde{K}_i = K_i/\lambda_{\mathrm{d}}$, and the potential for the fluctuations is given by

$$U = -\hat{l}_z^2 - (\hat{\mathbf{l}}\times\hat{\mathbf{d}}_0)^2 - \tilde{K}_6(\nabla\theta_0)^2 - (\tilde{K}_5 - \tilde{K}_6)(\hat{\mathbf{l}}\cdot\nabla\theta_0)^2. \tag{23}$$

The frequencies of the transverse resonance are determined by the eigenvalues $R_\perp^2 - 1$ as

$$\omega = \sqrt{\omega_0^2 + R_\perp^2\Omega_{\mathrm{A}}^2}, \tag{24}$$

where Ω_{A} is the A-phase longitudinal resonance frequency. An approximation for the lowest eigenvalue and the corresponding bound state of fluctuation can be obtained by the following variational principle:

$$R_\perp^2 - 1 = \min_{\psi}\frac{\int \mathrm{d}^3\mathbf{r}[\tilde{K}_6|\nabla\psi|^2 + (\tilde{K}_5 - \tilde{K}_6)|\hat{\mathbf{l}}\cdot\nabla\psi|^2 + U|\psi|^2]}{\int \mathrm{d}^3\mathbf{r}|\psi|^2}. \tag{25}$$

In a uniform state $\hat{\mathbf{d}} \parallel \hat{\mathbf{l}} \perp \mathbf{H}$, the absorption occurs at the bulk frequency given by $R_\perp^2 = 1$. However, dipole-unlocked regions (such as the soft cores of continuous vortices) where $\hat{\mathbf{l}}$ and $\hat{\mathbf{d}}$ are antiparallel define a potential well for the spin fluctuations. Usually this gives rise to bound states with frequencies corresponding to $R_\perp^2 < 1$.

2 Vortices and wetting in ^{4}He-II

One of the unusual properties of ^{4}He-II is complete wetting of most materials, *i.e.* a layer of fluid tends to cover all the exposed solid surfaces. In contrast, most fluids exhibit partial

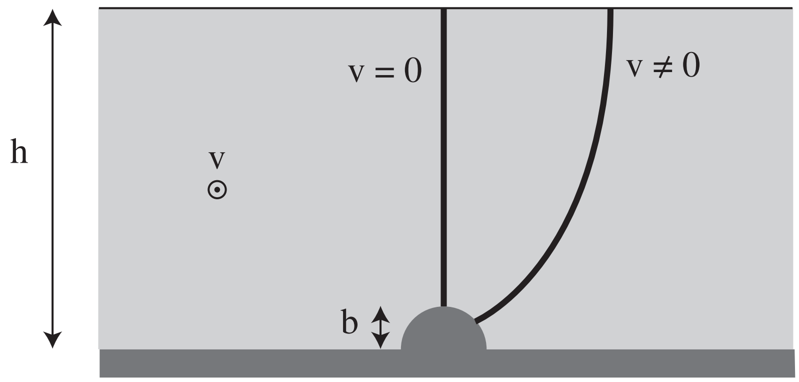

Figure 3: Pinning of a vortex line by a surface asperity of size $\sim b$ in a superfluid film of thickness h. The presence of a flow with velocity v causes the vortex to bend.

wetting by forming droplets, with characteristic contact angles defined by the interfaces separating the three phases (fluid, solid, vapour). Complete wetting thus corresponds to the vanishing of the contact angle. However, incomplete wetting by ^{4}He-II was predicted theoretically [25] and later confirmed experimentally on Cs surfaces [26]. Also, subsequent optical experiments displayed small contact angles, up to 15 mrad, on rough evaporated SiO_2 layers [27]. In publication [P1], a theoretical model based on an inhomogeneous distribution of vortices is investigated, with the purpose of explaining the experimental results observed in Ref. [27].

2.1 Vortex-pinning model

Vortices are present in practically all samples of ^{4}He-II, especially in thin films. Due to the small size of the core, they can easily become pinned by atomic-size imperfections on a rough solid surface. The presence of a flow in the film causes a pinned vortex to become bent (see Fig. 3), and finally unpinned when the velocity reaches a critical value [28]

$$v_{\mathrm{c}} = \frac{\kappa}{4\pi h} \ln\left(\frac{b}{a_0}\right), \tag{26}$$

where $\kappa = 2\pi\hbar/m_4$, h is the thickness of the film, b is a typical radius of the imperfections, and a_0 is of the order of the vortex core radius. At this velocity, the radius of curvature for the bending of the vortex falls below the film thickness. If the unpinning flow is assumed to arise from a neighboring vortex (with a velocity field $\propto 1/r$), the condition (26) provides a maximum density $n_{\max}$ of vortices. To logarithmic accuracy, this can be estimated as

$$n_{\max} = \frac{1}{4h^2}. \tag{27}$$

Therefore, a given density of vortices n can only be supported by sufficiently thin superfluid films, with $h < h_{\mathrm{t}} \equiv 1/(2\sqrt{n})$. This leads to the possibility of a spatially varying film thickness $h(\mathbf{r})$, caused by an inhomogeneous distribution of vortices. In the thin-film region, the vortex density n in our model is assumed to be given by the density of available pinning centers, while for $h > h_{\mathrm{t}}$ the vortices become unpinned, and their density follows Eq. (27). The transition region separating the areas with different film thicknesses can be characterized by a pseudo-contact angle (somewhat like the true contact angles in partial-wetting situations), derived from the maximum slope of the film profile.

2.2 Calculation of equilibrium film profile

The surface profile can be obtained by minimizing the free energy of the film. For simplicity, we assumed translational invariance in one coordinate along the solid surface, whereby the profile becomes a one-dimensional function $h(x)$. The free energy per unit length is given by

$$\frac{F_{\mathrm{film}}}{L} = \int dx \left[-\frac{A}{12\pi h^2} + \tfrac{1}{2}\rho g h^2 + \tfrac{1}{2}\sigma \left(\frac{dh}{dx} \right)^2 + \frac{\rho_{\mathrm{s}}\kappa^2}{4\pi} h n(h) \right]. \tag{28}$$

The first term accounts for the van der Waals interaction of vapour and solid across the helium film, approximated by the energy between two flat surfaces. For the Hamaker constant A we used the value measured for a CaF_2 surface [29]. Because $A < 0$, the helium film tends to thicken under the influence of the interaction. The second term is the gravitational energy of the film, and the third term is the surface tension for a weakly inhomogeneous profile. The final term is the kinetic energy of the vortices (again, to logarithmic accuracy), the density of which is taken to be divided into two regions,

$$n(h) = \begin{cases} n_0 & h < h_{\mathrm{t}} \\ 1/(4h^2) & h > h_{\mathrm{t}} \end{cases}, \tag{29}$$

where $h_{\mathrm{t}} = 1/(2\sqrt{n_0})$. The numerical values of the parameters used in the calculations can be found in [P1]. The balance between the van der Waals term and the gravitational term defines a characteristic film thickness $h_0 = [|A|/(6\pi\rho g)]^{1/4} \sim 700$ nm. Our model has two constant equilibrium solutions, h_1 and h_2 ($h_1 < h_0 < h_2$), corresponding to the local minima of (28) with the two expressions for the vortex density given by Eq. (29). For a given density n_0 of the pinning centers, two regions with different film thicknesses can exist whenever $h_1 < h_\mathrm{t} < h_2$. This condition effectively restricts the use of the model to a certain range $n_1 < n_0 < n_2$ (with the parameters in [P1], $n_1 = 3 \cdot 10^{10}$ m^{-2} and $n_2 = 1.9 \cdot 10^{15}$ m^{-2}).

In the numerical calculations, we employed a discrete lattice with N equally spaced points x_i ($i = 1, ..., N$). The surface profile was presented by its value $h_i = h(x_i)$ at these locations. The equilibrium profile for a given value of n_0 was determined by discretizing the free energy (28) and relaxing an initial profile towards decreasing energy, until the local minimum was reached. The minimization was performed under the condition that the volume of the liquid remains constant. For an inhomogeneous solution describing the thin-to-thick transition region, the pseudo-contact angle was determined through $\theta_\mathrm{p} = \arctan[\max(dh/dx)]$. For the density range 10^{11} m^{-2} $< n_0 <$ 10^{13} m^{-2}, the calculated pseudo-contact angles were distributed in the range 10 mrad $< \theta_\mathrm{p} <$ 40 mrad, in order-of-magnitude agreement with the apparent contact angles observed in the measurements of Ref. [27]

3 Flow stability in ^{3}He-A

Although the structure and stability of the current-carrying states in ^{3}He-A are widely discussed in literature (see *e.g.* [P2] for a list of references) and the processes responsible for the breakdown of the superflow have been known for a long time, most of this work has been done either by using analytical methods or by restricting the texture to follow the form of a variational ansatz. Accordingly, the authors have been forced to resort to a number of simplifications in their studies. As a result, some questions concerning the flow stability that have relevance in the interpretation of experimental observations have remained unanswered. The methods of numerical computation allow direct determination of the order-parameter texture, at least in simple geometries, without the need to make any restrictions concerning its form.

In this thesis, I have studied theoretically the critical velocity v_c of rectilinear flow in ^{3}He-A in bulk (publications [P2] and [P3]) and in parallel-plate geometry (publication [P4]). The results are compared with measured critical velocities $\Omega_\mathrm{c} R$ for vortex creation in a rotating cylinder (with a radius R). The calculations focus on the case where the external magnetic field $\mathbf{H}$ is perpendicular to $\mathbf{v}_\mathrm{s}$, as it is often the relevant orientation in

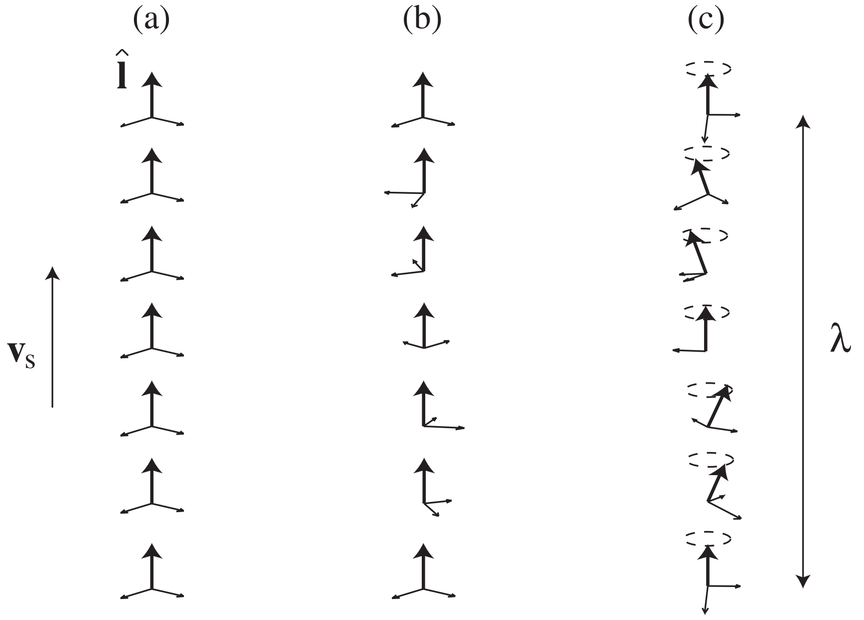

Figure 4: The orientation of the orbital triad in one-dimensional flow textures in ^{3}He-A: (a) the uniform texture with $v_\mathrm{s} = 0$, (b) the uniform texture with $0 < v_\mathrm{s} < v_\mathrm{c1}$ ($\hat{\mathbf{l}} \parallel \mathbf{v}_\mathrm{s}$), and (c) the helical texture for $v_\mathrm{s} > v_\mathrm{c1}$.

the experiments. In publication [P2], the critical velocities of the intrinsic flow instability in ^{3}He-A are determined, with a particular emphasis on the effects caused by the form of the underlying orbital texture $\hat{\mathbf{l}}(\mathbf{r})$. The dependences on temperature and magnetic field strength are also investigated. The results are compared with experimental data in publication [P3]. It should be emphasized that the comparison between theory and measurements can be done directly without any adjustable parameters. The effects of geometrical confinement due to the presence of lateral walls are studied in publication [P4]. In particular, the case with a domain wall stretched between the walls in the flow channel provides a model for the growth of a vortex sheet in ^{3}He-A.

3.1 Instability of the uniform texture

In the presence of a magnetic field $\mathbf{H}$ and vanishing superfluid velocity, the minimum of (17) corresponds to the uniform texture $\hat{\mathbf{l}}(\mathbf{r}) = \hat{\mathbf{d}}(\mathbf{r}) = \text{const.} \perp \mathbf{H}$, which is the simultaneous minimum of the gradient, dipole-dipole, and magnetic-field energies (see Fig. 4a). For nonzero H, this state persists as the minimum configuration also under a small imposed superfluid velocity $\mathbf{v}_\mathrm{s} \perp \mathbf{H}$ with $|\mathbf{v}_\mathrm{s}| < v_\mathrm{c1}$: the phase gradient corresponding to $\mathbf{v}_\mathrm{s}$ is achieved by turning $\hat{\mathbf{m}}$ and $\hat{\mathbf{n}}$ around a constant $\hat{\mathbf{l}}$ (Fig. 4b). The superfluid velocity only lifts the degeneracy in the mutual direction of $\hat{\mathbf{l}} = \hat{\mathbf{d}} \perp \mathbf{H}$ by favouring $\hat{\mathbf{l}} \parallel \mathbf{v}_\mathrm{s}$, because this orientation minimizes the anisotropic kinetic energy ($\rho_\parallel < \rho_\perp$), see Eq. (16). However, if the velocity is raised beyond the first critical velocity $v_{\mathrm{c}1}$ (of the order of the dipole velocity v_d), the uniform texture becomes unstable towards small-amplitude transverse fluctuations (Fig. 4c) [30]. The resulting helical texture has $\hat{\mathbf{l}}$ winding around the direction of the superfluid velocity with a characteristic wave number $q = 2\pi/\lambda$, where λ (a few times ξ_d) is the wavelength of a helix. The reason for the appearance of these deformations lies in the coupling between the velocity field and an inhomogeneous orbital texture in Eq. (16).

Helical textures in ^{3}He-A have been subject to extensive investigation in the past, but usually assuming the field orientation $\mathbf{H} \parallel \mathbf{v}_\mathrm{s}$. In this case, the magnetic field and the superflow impose competing influences on the order-parameter texture, destabilizing the uniform configurations. In contrast, when $\mathbf{H} \perp \mathbf{v}_\mathrm{s}$, both magnetic and kinetic energies can be minimized simultaneously, leading to higher critical velocities for the breakdown of the uniform texture. In addition, this case is theoretically more challenging because the magnetic field breaks the rotational invariance around $\mathbf{v}_\mathrm{s}$, introducing “easy” and “hard” directions for the fluctuations. Consequently, the resulting helical texture is elliptically distorted (the end of the winding $\hat{\mathbf{l}}$ vector traces an ellipse instead of a circle).

After their formation, the subsequent fate of the helical textures depends crucially on the values of the various parameters in Eq. (16). These in turn depend on the external conditions, most notably temperature and pressure. The important question is whether the instability of the uniform state at $v_{\mathrm{c}1}$ leads to a stable helical texture or to a dissipative situation accompanied by the degradation of the mass supercurrent, the density of which can be written

$$\mathbf{j}_\mathrm{s} = \rho_\perp \mathbf{v}_\mathrm{s} + (\rho_\parallel - \rho_\perp)\hat{\mathbf{l}}(\hat{\mathbf{l}} \cdot \mathbf{v}_\mathrm{s}) + C\nabla \times \hat{\mathbf{l}} - C_0 \hat{\mathbf{l}}(\hat{\mathbf{l}} \cdot \nabla \times \hat{\mathbf{l}}). \tag{30}$$

It turns out that, depending on the external parameters, it is possible to obtain stable helical textures, which become finally unstable at a second critical velocity $v_{\mathrm{c}2} \geq v_{\mathrm{c}1}$. The structure and stability of helical textures in the case $\mathbf{H} \perp \mathbf{v}_\mathrm{s}$ have been previously studied only by Lin-Liu *et al.* in Ref. [31]. However, they consider only the limiting case of the immediate vicinity of $T = T_\mathrm{c}$ (the Ginzburg-Landau regime). In publication [P2], this investigation is extended to lower temperatures.

3.2 Calculations on helical textures

In the numerical calculations, the order parameter was assumed to depend only on the coordinate x along the direction of the superfluid velocity, and defined on N equidistant points in the interval $-L/2 < x < L/2$. Concerning the initial instability of the uniform texture, it has been proven [31] that the longitudinal fluctuations are the relevant ones; this is expected to be true also in considering the stability of the helical textures. The superflow is generated by keeping a fixed difference in the order-parameter phase $\Delta\Phi = \Phi(L/2) - \Phi(-L/2)$ over the interval. Although a well-defined phase function $\Phi(x)$ only exists when $\hat{\mathbf{l}}$ is confined to a plane (which clearly does not hold with helical textures), it is still possible to keep a constant phase difference $\Delta\Phi$ in the calculations with the following procedure. The calculation begins with an initial configuration (as in Fig. 4b)

$$\hat{\mathbf{m}}_0 + i\hat{\mathbf{n}}_0 = (\hat{\mathbf{y}} + i\hat{\mathbf{z}})e^{i(\Delta\Phi/L)x}, \tag{31}$$

which corresponds to a situation with a constant driving velocity $\mathbf{v} = [\hbar/(2m_3)](\Delta\Phi/L)\hat{\mathbf{x}}$. As the configuration is iterated (in fictitious time t) towards the minimum of the discretized free energy, the phase difference $\Delta\Phi$ is kept constant at every iteration step by imposing a boundary condition

$$\left(\hat{\mathbf{m}} \cdot \frac{d\hat{\mathbf{n}}}{dt}\right)_{x=-L/2} = \left(\hat{\mathbf{m}} \cdot \frac{d\hat{\mathbf{n}}}{dt}\right)_{x=L/2}. \tag{32}$$

Actually, the initial configuration was chosen to contain a small disturbance in the middle of the interval. For small enough phase differences, corresponding to $v < v_{\mathrm{c1}}$, the converged solution had the uniform structure, whereas for $v > v_{\mathrm{c1}}$ the disturbance developed into a helical texture.

In the case of a long channel, $L \gg \xi_{\mathrm{d}}$, the wave vector q of the helical texture can adjust to minimize the free energy. Therefore q has to be considered as a variable in the calculations. Taking into account the periodicity of the problem, the calculations were restricted to a single wavelength of the helix. Minimization with respect to the texture parameters at a given v and wave vector q leads to a free-energy function of two variables $F(v, q)$. The stability of the helical textures is determined by the eigenvalues of the Hessian matrix

$$\mathcal{H} = \begin{pmatrix} \frac{\partial^2 F}{\partial v^2} & \frac{\partial^2 F}{\partial v \partial q} \\ \frac{\partial^2 F}{\partial v \partial q} & \frac{\partial^2 F}{\partial q^2} \end{pmatrix}. \tag{33}$$

For stability, both of the eigenvalues of $\mathcal{H}$ have to be positive. The second critical velocity $v_{\mathrm{c}2}$ can now be defined as the lowest value of v with which the helical texture corresponding to the optimally chosen wave vector q_{opt} becomes unstable. The instability at $v_{\mathrm{c}2}$ leads to the breakdown of superflow through the creation of continuous doubly-quantized vortices, thus reducing the flow to a subcritical value.

In publication [P2], the stability regions and the detailed structure of the helical textures are presented. For the first time, we studied the dependence on temperature. An extended stability region of helical textures in the presence of a magnetic field $H \gg H_{\mathrm{d}}$ was found at temperatures $T < 0.8\ T_{\mathrm{c}}$. We also found that the critical velocities $v_{\mathrm{c}2}$ for the instability of the helical textures coincide reasonably well with the largest observed critical velocities for vortex formation in a rotating cylinder, see publication [P3].

3.3 Flow in the presence of solitons

The above discussion on the helical textures applies to the case where the initial flow state is homogeneous. However, stable inhomogeneities can exist in the texture because of the complicated order-parameter structure of ^{3}He-A. Obviously, the presence of such inhomogeneities can cause significant reductions in the critical velocity of the superflow. The one-dimensional flow model enables us to study a group of commonly encountered defects called solitons.

Solitons are planar domain-wall-like objects that separate two energetically degenerate equilibrium states. Planar defects owe their existence to a twofold degeneracy of some interaction. For example, the dipole-dipole energy (14) in ^{3}He-A has a minimum when either $\hat{\mathbf{l}} = \hat{\mathbf{d}}$ or $\hat{\mathbf{l}} = -\hat{\mathbf{d}}$. In a dipole-unlocked soliton, two regions with parallel and antiparallel asymptotic orientations of $\hat{\mathbf{l}}$ and $\hat{\mathbf{d}}$ are connected by a wall-like transitional area with a thickness of $\sim \xi_{\mathrm{d}}$, where the angle between the vectors changes continuously from 0 to 180°. The dipole-unlocked soliton is stable since its removal would require a large amount of energy. In the presence of flow, another soliton structure, the dipole-locked soliton, becomes possible. In this case, the doubly degenerate interaction is provided by the anisotropic kinetic energy, minimized when $\hat{\mathbf{l}} = \mathbf{v}_{\mathrm{s}}$ or $\hat{\mathbf{l}} = -\mathbf{v}_{\mathrm{s}}$.

A soliton texture responds to the applied flow by rotating as a whole around the flow direction. As an example, consider a dipole-unlocked soliton in the presence of a constant driving velocity $\mathbf{v} \parallel \hat{\mathbf{x}}$, with asymptotic orientations $\hat{\mathbf{l}} = \pm\hat{\mathbf{x}}$, $x \to \pm\infty$ (see Fig. 5). If the texture is rotated by an angle θ around $\hat{\mathbf{x}}$, the phase difference $\Delta\Phi$ along the x axis changes by 2θ. The final state carries zero mass current, as calculated from Eq. (30). Therefore, if

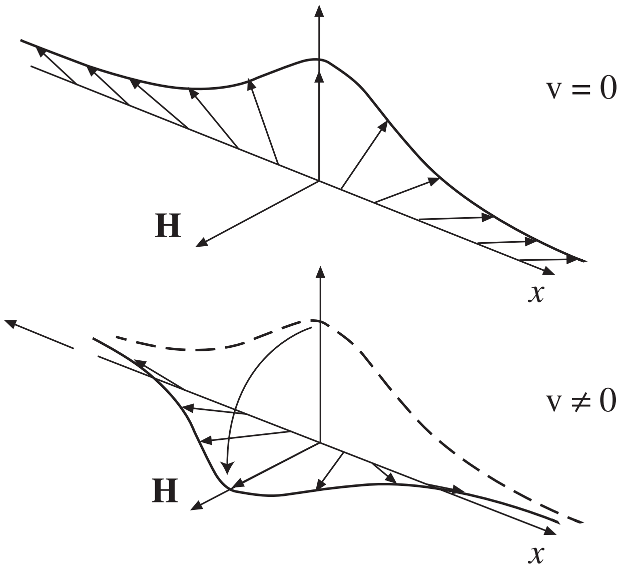

Figure 5: The variation of $\hat{\mathbf{l}}$ in a one-dimensional soliton texture. When an external flow is applied, the soliton tends to detach from the plane perpendicular to the external field $\mathbf{H}$.

nothing prevents this rotation, any phase difference can be produced by choosing a suitable angle θ, and the critical velocity of the superflow vanishes for the soliton. However, in the presence of a magnetic field $\mathbf{H} \perp \mathbf{v}_\mathrm{s}$, the rotation of $\hat{\mathbf{l}}$ is opposed by the field through the dipole coupling to $\hat{\mathbf{d}} \perp \mathbf{H}$. Therefore, for small driving velocities, a nonzero supercurrent $j_{\mathrm{s},x}(v)$ is built up by the induced nonplanarity of $\hat{\mathbf{l}}(x)$, see the bottom of Fig. 5. Finally, as the critical velocity is exceeded, the texture becomes unstable against unlimited winding around $\hat{\mathbf{x}}$, accompanied by an abrupt drop in the supercurrent.

In publication [P2], we determine the critical velocities for both dipole-locked ($\hat{\mathbf{l}} \approx \hat{\mathbf{d}}$) and dipole-unlocked ($\hat{\mathbf{d}} \approx$ const.) solitons numerically as a function of temperature and the strength H of the applied field. Apart from the choice of the initial configurations, the calculations are carried out in a similar fashion as in the case of uniform textures, explained in Section 3.1. We found that the lowest critical velocities are associated with the dipole-unlocked solitons, with $v_{\mathrm{c,US}}$ roughly a factor of six smaller than v_{c2} of the originally uniform texture. The large spread compares very well with experimental observations of the A-phase critical velocities in a rotating cylinder with different histories of flow-state preparation. The comparison, presented in publication [P3], supports the view that the critical velocity in ^{3}He-A reflects the instability of the bulk flow, and depends on the underlying orbital texture.

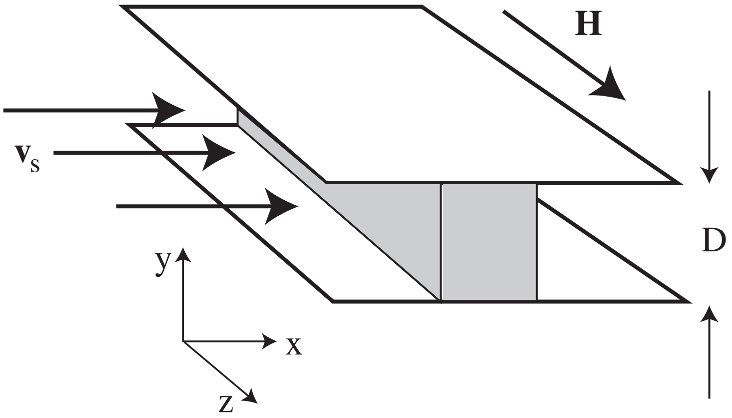

Figure 6: The parallel-plate geometry with the plate separation D and the superfluid velocity $\mathbf{v}_s$ in the positive x direction. The orientations of the external magnetic field $\mathbf{H}$ and the soliton wall (grey) are also shown.

3.4 Uniform flow between walls

In studying the one-dimensional bulk flow, as described in Secs. 3.1 – 3.3, the finite size of the container is not taken into account. Publication [P4] investigates the effects of confinement on the critical velocity of ^{3}He-A. We used a flow channel consisting of two parallel plates separated by a distance D, and studied the field orientation $\mathbf{H} \perp \mathbf{v}_s$. Our main goal was to investigate the flow in the presence of a dipole-unlocked soliton stretched between the plates. The instability of the soliton provides a plausible model for the experimentally measurable growth of a vortex sheet as a function of $\mathbf{v}_s$. In publication [P4], we calculated the order-parameter texture in ^{3}He-A in the presence of flow for the first time in two spatial dimensions.

The numerical calculations in [P4] (see Fig. 6) used a discrete lattice in the xy plane with a length L in the direction of the flow ($-L/2 < x < L/2$) and width D in the y direction ($-D/2 < y < D/2$). Translational invariance in the z direction was assumed, and the magnetic field $\mathbf{H} \parallel \hat{\mathbf{z}}$ was assumed to force $\hat{\mathbf{d}}$ to vary in a plane with $\hat{d}_z = 0$. For simplicity, the calculations were restricted to the Ginzburg-Landau region. The order parameter was taken to be defined at $N \times M$ points spaced by Δx and Δy in x and y directions, respectively ($N\Delta x = L$, $M\Delta y = D$). The equilibrium distribution was determined by minimizing the total energy consisting of the dipole-dipole and gradient contributions. The superflow was generated by keeping a fixed difference $\Phi(x = L/2) - \Phi(x = -L/2) \equiv \Delta\Phi$ in the order-parameter phase in the x direction. For different values of $\Delta\Phi$, we monitored the average supercurrent density

$$j \equiv \langle j_{s,x} \rangle = \frac{1}{D} \int_{-D/2}^{D/2} \mathrm{d}y \, j_{\mathrm{s},x}(x,y), \tag{34}$$

as a function of the driving velocity $v = [\hbar/(2m_3)](\Delta\Phi/L)$.

In the absence of flow, the simplest order-parameter texture in equilibrium has uniform $\hat{\mathbf{l}} = \hat{\mathbf{d}}$ perpendicular to the walls and the external magnetic field. This state persists even under a small induced velocity v, resulting in a current $j = \rho_\perp v$ (because $\hat{\mathbf{l}} \perp \mathbf{v}_\mathrm{s}$). As the velocity exceeds the limiting value v_Fr, approximatively satisfying the relation

$$v_\mathrm{Fr} = \frac{c}{D} \tag{35}$$

with c=constant, the texture undergoes a Freedericksz transition [32]. After the transition, $\hat{\mathbf{l}}$ begins to tilt towards the flow direction in the middle of the channel, to reduce the anisotropic kinetic energy, still retaining the invariance in the coordinate along the flow. The numerical value of c depends on the behaviour of $\hat{\mathbf{d}}$: if $D \ll \xi_\mathrm{d}$, $\hat{\mathbf{d}}$ stays constant, whereas in the other limit $D \gg \xi_\mathrm{d}$ dipole-locking forces $\hat{\mathbf{d}}$ to follow $\hat{\mathbf{l}}$, providing the texture with additional rigidity. Our values of v_Fr calculated in publication [P4] are in agreement with previously published work [33].

If v is increased further, $\hat{\mathbf{l}}$ continues tilting until it is, apart from the immediate vicinity of the walls, almost aligned with the superfluid velocity. This situation is a generalization of the preceding discussion on one-dimensional flow. Therefore, a helical instability is expected to occur also in this case. Indeed, we observed the transition in the numerical calculations, with the critical velocity v_h satisfying an approximate relation

$$v_\mathrm{h}(D) \approx v_\mathrm{c1} + \frac{a}{D^2}, \tag{36}$$

where v_c1 is the critical velocity for the formation of helical textures in the one-dimensional model ($D \to \infty$) and a is a constant. Consequently, the presence of confining walls modifies the critical velocity in the uniform flow state only slightly.

3.5 Vortex sheet growth

The main interest in studying ^{3}He-A flow between parallel plates is provided by a close analogy to the measurements in a rotating cylinder in the presence of a vortex sheet. The vortex sheet is a planar object consisting of a dipole-unlocked soliton that carries quanta of continuous vorticity (see Fig. 7) [34]. On increasing the angular velocity of

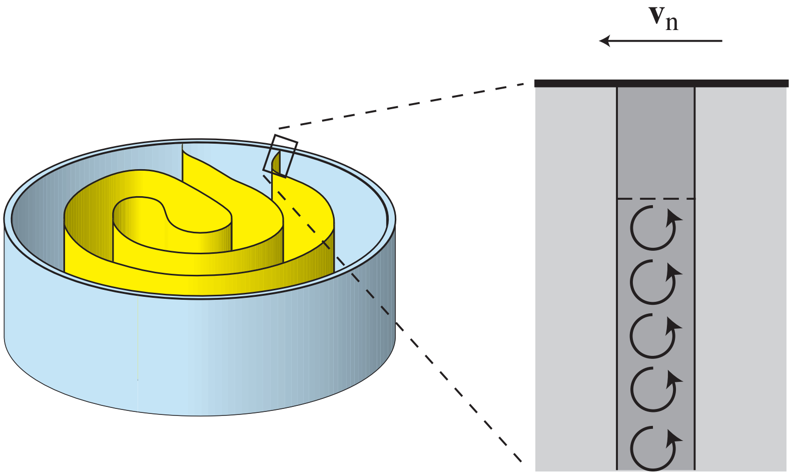

Figure 7: Schematic representation of a vortex sheet. The sheet is attached to the container wall by a soliton piece that carries no vorticity.

rotation, additional vortex quanta enter the sheet, as the counterflow velocity through the vortex-free soliton piece exceeds a critical value. As new vorticity is added, the sheet grows in length. In publication [P4], we used the channel-flow model in the presence of a dipole-unlocked soliton (Fig. 6) to determine the critical velocity for vortex-sheet growth.

The calculations with the soliton follow the same lines as described in Sec. 3.4 in connection with uniform flow, except that the driving velocity has to be incorporated in the model with some caution due to the breaking of translational invariance. Apart from the additional rigidity caused by the anchoring of $\hat{\mathbf{l}}$ at the walls, the instability of the soliton also occurs through a similar process of texture rotation as in the bulk case. The critical velocity v_c (or, equivalently, the critical phase difference $\Delta\Phi$) for the instability turned out to depend quite strongly on the chosen length L of the computational region. To avoid time-consuming numerical calculations on large lattices, we determined the critical current j_c instead, since it was observed to show a weaker L dependence. The corresponding velocity v_c can then be obtained from the $j(v)$ diagram for the uniform flow channel.

In publication [P4], we present the critical velocity $v_\mathrm{c}(D)$ for the soliton instability as a function of the plate separation D. At the bulk limit, $D \gg \xi_\mathrm{d}$, our results reproduce the low value of $v_\mathrm{c,US}$ determined for the one-dimensional flow in publication [P2]. This should be emphasized since a much higher value has been calculated previously [35]. However, our low values are supported by the experimentally measured critical velocities for the vortex sheet [22]. Also, the critical current was found to show a more pronounced D

dependence than the uniform-flow case, following an approximate relation

$$j_{\mathrm{c}} \approx \frac{a}{D} + b, \tag{37}$$

with different constants a and b above and below the Freedericksz transition. Although the constant-velocity model is a somewhat crude approximation for the inhomogeneous velocity distribution in a rotating cylinder, it explains qualitatively the Ω dependence of v_{c} observed in the experiments of Ref. [22].

In addition, we determined the NMR frequency shift $R_{\perp}^2$ of the dipole-locked soliton in the presence of flow by solving numerically the minimization problem of Eq. (25). At the limit of large D, the lowest eigenmodes were found to be concentrated at the contact points of the soliton and the walls. The values of $R_{\perp}^2$ were found to be considerably lower than those calculated previously for a bulk soliton, emphasizing the important role played by the container walls. In fact, the values are rather close to those expected for the vortex sheet itself [34], and thus the wall connections are not expected to generate a separately distinguishable satellite. This conclusion agrees with measurement.

4 Vortices and NMR in ^{3}He-B

In ^{3}He-B, the length scale of the order-parameter textures is determined by the long magnetic coherence length $\xi_{\mathrm{H}} \sim 1$ mm. This is of the same order of magnitude as the radius R of a typical sample cylinder in rotating experiments. Therefore, in contrast to ^{3}He-A where the relevant length scale $\xi_{\mathrm{d}} \ll R$ and all the calculations necessarily are of local nature, the B-phase texture must be determined over the entire sample. In publication [P5], I calculated the equilibrium texture and the corresponding NMR line shape in a rotating cylinder. The model is developed to a level where a direct comparison with the experimentally obtained NMR spectra is possible. The effects of metastable rotating states (*i.e.* states with a nonequilibrium number of vortices) are included in the model. Special emphasis is given on how the sensitivity to the number of vortices in the cylinder depends on the external parameters controlling the behaviour of the system. In publication [P6], I used a similar procedure to predict the NMR response in the presence of a spin-mass vortex.

4.1 Line shapes of flare-out textures

The spatial distribution of $\hat{\mathbf{n}}$ can be determined by finding the minimum for the sum of different energy contributions given by Eqs. (8)–(13). In the presence of a large magnetic field $H \gg H_{\rm d}$, the equilibrium texture in the infinitely long cylinder has the rotationally symmetric flare-out form [16], *i.e.* the components of $\hat{\mathbf{n}}$ expressed in the cylindrical coordinate system only depend on the radial coordinate r. The remaining one-dimensional texture problem is solved by discretization methods. The NMR spectrum corresponding to the texture variations can then be obtained from the distribution $\beta(r)$ of the angle between $\hat{\mathbf{n}}$ and the axial magnetic field $\mathbf{H}$ through Eqs. (20) and (21).

As pointed out in Sec. 1.4, the critical velocity for the nucleation of vortices in ^{3}He-B is large. Therefore, it is possible to study a vortex-free state in a cylinder over a considerable range of rotation velocities Ω. Because the superfluid component remains then stationary, the rotation generates a counterflow $v(r) = \Omega r$, which in turn affects the texture through the flow-energy term (9). However, if the sample has been prepared with a certain number N of vortices, situated in a central bundle at the cylinder axis, the counterflow velocity becomes modified by the superfluid velocity field of the vortices. Inside the bundle, the average superfluid velocity $\langle \mathbf{v}_{\rm s} \rangle \approx \mathbf{v}_{\rm n}$ and the counterflow vanishes, whereas in the vortex-free counterflow annulus $v(r) = \Omega r - \Omega_{\rm V} R^2/r$, where $\Omega_{\rm V} = \Omega N/N_0$, and $N_0 = 2\pi R^2 \Omega/\kappa_0$ is the vortex number for the completely filled container [vortices distributed with equilibrium density given by Eq. (19)].

As the rotation velocity Ω is increased in the vortex-free case, the equilibrium state undergoes a sequence of textural transitions [36], with typical associated NMR line shapes presented in Fig. 8. The main features of these line shapes can be understood by the accumulation at two distinct frequencies: the Larmor frequency (given by $\sin^2\beta = 0$) that represents the minimum of the magnetic-field energy (8), and the frequency of counterflow ($\sin^2\beta = 0.8$) corresponding to the minimum of Eq. (9). Roughly speaking, at low rotation velocities, most of the absorption occurs at the Larmor peak [apart from the tail caused by the surface energy (11)] and, as Ω is increased, the absorption gradually shifts to the counterflow peak. If vortices are present in the container, they reduce the counterflow, decreasing the counterflow peak height.

However, the actual measured NMR spectra are subject to other sources of line broadening besides that caused by the texture. The inhomogeneity of the static magnetic field H is one of them. Spatial variations in the field strength induce a spread in the Larmor frequency and, consequently, in the resonance frequency of Eq. (20). Another source of

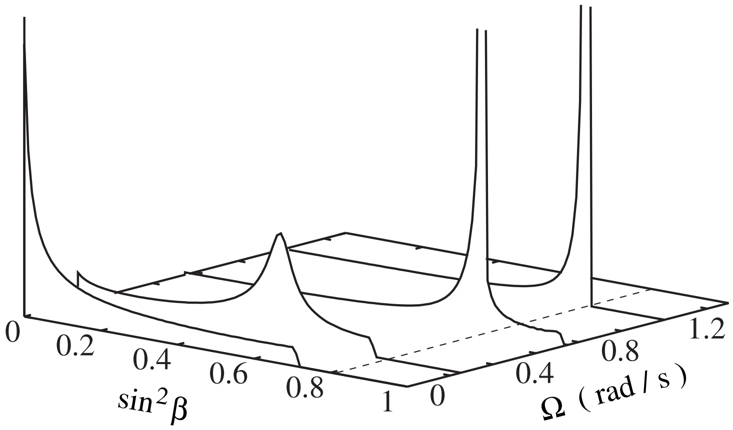

Figure 8: Calculated texture-induced NMR line shapes as a function of the rotation velocity Ω.

line broadening is the intrinsic Leggett-Takagi relaxation, arising from the nonequilibrium between the normal and superfluid contributions to the total magnetization [37]. With the inclusion of these two mechanisms, we could reproduce the main features of the observed line shapes. Our procedure involves only one unknown fitting parameter, the Leggett-Takagi relaxation time τ_{LT}. The values of τ_{LT} corresponding to the best fit are in agreement with existing measurements [38]. The average magnetic-field inhomogeneity was determined from the signal of the normal-phase resonance. These were the first optimization calculations where line-broadening effects have been taken into account and where the calculated and measured line shapes could be compared, not only in terms of frequency shifts, but also with respect to relative absorption intensities.

At sufficiently large rotation velocities, the counterflow peak is the main characteristic feature of the line shape (see Fig. 8). In publication [P5], we calculated the height of this peak as a function of external conditions: magnetic field strength, angular velocity, temperature, and the number of vortex lines. With a single fitting parameter τ_{LT}, reasonable agreement was achieved in the comparison. Because the two additional line-broadening mechanisms have different dependences on the magnetic field strength, an optimal value for H (corresponding to minimal broadening) can be exctracted from our model. In [P5], we also studied the effects related to the finite length of the cylinder by calculating the texture in two spatial dimensions. In this work, the entire order-parameter texture of ^{3}He-B in a finite cylinder was determined for the first time.

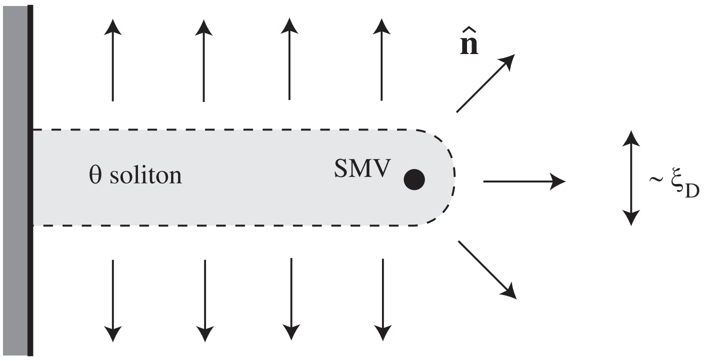

Figure 9: Schematic representation of a spin-mass vortex with a soliton tail.

4.2 NMR and a spin-mass vortex

In publication [P6], we used the model developed in [P5] to calculate the NMR response due to a presence of one spin-mass vortex in a rotating cylinder. A spin-mass vortex (SMV) is a composite object of three different defects of the B-phase order-parameter field. It consists of two linear vortices, an ordinary mass vortex and a spin vortex (surrounded by a circulating spin current), sharing a common core, and a planar tail formed by a soliton. The soliton tail connects the SMV to the wall of the rotating container, see Fig. 9. These defects can be found in specially prepared rotating states of ^{3}He-B [39, 40]. Their experimental identification is based on the specific NMR signature induced by the soliton wall. Inside the soliton, the rotation angle θ of the order parameter deviates from the minimum of the dipole energy. Therefore, its width is of the order of ξ_D, and much smaller than the length scale of the $\hat{\mathbf{n}}$ textures. Nevertheless, despite its small size, a single soliton can be observed because it fixes $\hat{\mathbf{n}}$ parallel to its normal vector, as shown in Fig. 9. The texture regains the flare-out structure at a distance of $\sim \xi_\mathrm{H}$ from the SMV. This results in increased absorption at high frequencies, corresponding to $\sin^2\beta \approx 1$.

The surface tension of the soliton wall is stabilized by the counterflow-induced Magnus force acting on the SMV. In the presence of a vortex bundle (of radius R_V), the SMV is located at its edge. If the rotation velocity is increased, the radius of the bundle decreases according to $R_\mathrm{V} \propto \Omega^{-1/2}$, and the soliton grows in length. Therefore, the amount of increased absorption at high frequencies was expected to increase as well. To estimate this effect, we determined numerically the equilibrium order-parameter texture in the cylinder with the soliton wall. The order parameter was calculated in a two-dimensional cross section of the cylinder (neglecting the dependence on the coordinate z along the axis) using a discrete lattice in the polar coordinates r and ϕ. The same energy contributions were taken into account as in publication [P5], explained in Sec. 4.1. The NMR response was determined by the same method as in [P5].

Contrary to the initial expectations, our calculations indicated a slight decrease in the additional high-frequency absorption when Ω was increased. This can be understood by taking into account the decrease in the characteristic length over which the texture returns to the flare-out form. Another unexpected feature is a textural transition from a slightly modified flare-out state to a different, roughly reflection-symmetric $\hat{\mathbf{n}}$ texture. In this new state, most of the absorption accumulates at the high frequencies. Our calculations suggest that, for suitably chosen external conditions, this transition could be triggered by increasing Ω, with critical velocities well within the reach of rotating cryostats. So far this transition has not been experimentally searched for.

5 Summary

This thesis has investigated theoretically vortex-related phenomena in superfluids. The following summarizes the main results.

In ^{4}He-II, vortices pinned by surface irregularities can give rise to a spatially varying film profile on a solid substrate [P1], providing an interpretation for the small apparent contact angles observed in optical experiments.

Superfluid ^{3}He is an exceptional system in that it exhibits several highly nontrivial phenomena, which can be investigated both experimentally and theoretically. Unlike its counterparts *e.g* in the field of superconductivity, it is free of impurities and has no crystalline lattice or other constraints except for the external boundary. All the complexity in its behaviour arises from the symmetry and structure of the order parameter. Thus the properties of the superfluid phases of ^{3}He can, in principle, be calculated, if proper care is taken in the choice of models.

In superfluid ^{3}He-A, the stability of rectilinear superflow was studied numerically in bulk [P2,P3] and in the presence of confining walls [P4] using the hydrostatic theory. The critical velocities for the formation of doubly-quantized continuous vortices were determined as a function of temperature and external magnetic field. Our results indicate a pronounced dependence on the structure of the underlying order-parameter field, explaining the large spread of the critical velocities observed in experiments using a rotating cryostat. Our model employing a soliton wall stretched between two parallel walls reproduces the main experimental features concerning the critical velocity in the presence of a vortex sheet.

The detailed NMR line shape of ^{3}He-B in a rotating cylinder was calculated numerically [P5]. With a single fitting parameter, our model explains satisfactorily the observed dependences on temperature, magnetic-field strength, rotation velocity, and the number of vortices in the sample. Our model suggests an optimal choice for the magnetic field so that maximum sensitivity to changes in the vortex number can be achieved. Our calculations also predict new features in the NMR response of a spin-mass vortex [P6]. In publications [P2-P6], the exact order-parameter distributions for both the A and B phases under externally applied flow were determined in one-dimensional and, for the first time, in two-dimensional geometries.

All the results obtained in this thesis reflect a high level of agreement between theory and experiment. With the help of modern computational tools, many fascinating and highly nontrivial phenomena exhibited by superfluid systems become available for investigation in full detail.

6 Publications

This thesis is based on the following original publications.

- [P1] R. Luusalo, A. Husmann, J. Kopu, and P. J. Hakonen, "Pseudo-contact Angle due to Superfluid Vortices in ^{4}He", Europhys. Lett. **50** (2), 222-228 (2000).
- [P2] J. Kopu, R. Hänninen, and E. V. Thuneberg, "One-dimensional Textures and Critical Velocity in Superfluid ^{3}He-A", Phys. Rev. B **62**, 12374-12380 (2000).
- [P3] V. M. H. Ruutu, J. Kopu, M. Krusius, Ü. Parts, B. Plaçais, E. V. Thuneberg, and W. Xu, "Critical Velocity of Vortex Nucleation in Rotating Superfluid ^{3}He-A", Phys. Rev. Lett. **79**, 5058-5061 (1997).
- [P4] J. Kopu and E. V. Thuneberg, "Soliton-limited Superflow in ^{3}He-A Between Parallel Plates", accepted for publication in J. Low Temp. Phys.
- [P5] J. Kopu, R. Schanen, R. Blaauwgeers, V. B. Eltsov, M. Krusius, J. J. Ruohio, and E. V. Thuneberg, "NMR Line Shape of Rotating ^{3}He-B at Large Counterflow Velocity", J. Low Temp. Phys. **120**, 213-232 (2000).
- [P6] J. Kopu and M. Krusius, "Spin-mass Vortex in ^{3}He-B: Order-parameter Texture and NMR Signature", Report TKK-KYL-005 (2000), submitted to Phys. Rev. B.

The author's own contribution:

The research work reported in this thesis is the result of collaboration between theorists and experimentalists. Together with my thesis supervisor, Docent Erkki Thuneberg, I formulated the mathematical models for describing the experimental situations. I implemented and performed most of the numerical calculations in [P1] and [P2], and all the calculations in [P3]–[P6]. I wrote the main part of [P2] and [P5] (excluding the description of measurements). Publications [P4] and [P6] were written by me.

Acknowledgments

I wish to express my gratitude to the two directors of the Low Temperature Laboratory, Academician Olli Lounasmaa and Professor Mikko Paalanen, for giving me the opportunity to work in the interesting field of low temperature physics.

I am deeply grateful for the excellent guidance provided by my supervisor, Docent Erkki Thuneberg. His expert ability to identify the essential physics behind the mathematical models and optimistic attitude in dealing with difficulties have been invaluable. I also want to thank the leaders of the experimental groups, Professors Matti Krusius and Pertti Hakonen, for their extraordinary enthusiasm and endless interest towards my work. I am indebted to my experimental co-authors and colleagues Rob Blaauwgeers, Vladimir Eltsov, Anke Husmann, Ülo Parts, Bernard Plaçais, Jaakko Ruohio, Ville Ruutu, Roch Schanen, Reeta Tarkiainen, and Wen Xu.

My special thanks go to my long-time room mates, theory-group colleagues and friends Risto Hänninen and Janne Viljas for excellent company during many years of work and an incalculable number of coffee breaks.

I have benefited from discussions with Marko Heinilä, Janne Karimäki, Tauno Knuuttila, Nikolai Kopnin, Juha Martikainen, Jari Penttilä, Leif Roschier, and Grigori Volovik. Also, I wish to thank my pre-examiners, Mikael Fogelström and Mikko Saarela, for reviewing my thesis.

I am grateful to the administrative staff Teija Halme, Marja Holmström, Pirjo Kinanen, Tuire Koivisto, Satu Pakarinen, and Liisi Pasanen for their help in practical matters. I thank the whole staff of the Low Temperature Laboratory for a friendly and inspiring atmosphere. Financial support from the Väisälä Foundation, Helsinki University of Technology, and the Finnish Cultural Foundation is gratefully acknowledged.

I thank my brother Janne for his expert help with computer graphics, and my parents, other relatives and friends for support. Finally, I wish to thank my dear wife Minna for much-needed help and encouragement during the final stages of preparing this thesis.

Otaniemi, March 2001

Juha Kopu

References

[1] D. R. Tilley and J. Tilley, *Superfluidity and Superconductivity*, (Adam Hilger, Bristol, 1990).

[2] A. J. Leggett, Rev. Mod. Phys. **47**, 331 (1975).

[3] D. Vollhardt and P. Wölfle, *The Superfluid Phases of ^{3}He*, (Taylor & Francis, London, 1990).

[4] V. P. Mineev, Usp. Fiz. Nauk **139**, 303 [Sov. Phys. Usp. **26**, 160] (1983).

[5] G. E. Volovik, *Exotic Properties of Superfluid ^{3}He*, (World Scientific, Singapore, 1992).

[6] M. M. Salomaa and G. E. Volovik, Rev. Mod. Phys. **59**, 533 (1987); Erratum: *ibid.* **60**, 573 (1988).

[7] O. V. Lounasmaa and E. Thuneberg, Proc. Natl. Acad. Sci. USA **96**, 7760 (1999).

[8] V. P. Mineyev and G. E. Volovik, Phys. Rev. B **18**, 3197 (1978).

[9] R. J. Donnelly, *Quantized Vortices in Helium II*, (Cambridge University Press, 1991).

[10] J. P. Pekola, J. T. Simola, P. J. Hakonen, M. Krusius, O. V. Lounasmaa, K. K. Nummila, G. Mamniashvili, R. E. Packard, and G. E. Volovik, Phys. Rev. Lett. **53**, 584 (1984).

[11] E. V. Thuneberg, Phys. Rev. Lett. **56**, 359 (1986).

[12] M. M. Salomaa and G. E. Volovik, Phys. Rev. Lett. **51**, 2040 (1983).

[13] Y. Kondo, J. S. Korhonen, M. Krusius, V. V. Dmitriev, E. V. Thuneberg, and G. E. Volovik, Phys. Rev. Lett. **68**, 3331 (1992).

[14] N. D. Mermin and T.-L. Ho, Phys. Rev. Lett. **36**, 594 (1976).

[15] Ü. Parts, J. M. Karimäki, J. H. Koivuniemi, M. Krusius, V. M. H. Ruutu, E. V. Thuneberg, and G. E. Volovik, Phys. Rev. Lett. **75**, 3320 (1995).

[16] H. Smith, W. F. Brinkman, and S. Engelsberg, Phys. Rev. B **15**, 199 (1977).

[17] E. V. Thuneberg, J. Low Temp. Phys. **122**, 657 (2001).

[18] W. F. Brinkman and M. C. Cross, in *Progress in Low Temperature Physics*, Vol. VIIA, ed. D. F. Brewer (North-Holland, 1978), p. 105.

[19] W. Zhang, J. Kurkijärvi, and E. V. Thuneberg, Phys. Rev. B **33**, 5124 (1986).

[20] A. D. Gongadze, G. E. Gurgenishvili, and G. A. Kharadze, Fiz. Nizk. Temp. **7**, 821 (1981) [Sov. J. Low Temp. Phys. **7**, 397 (1981)].

[21] J. W. Serene and D. Rainer, Phys. Rep. **101**, 221 (1983).

[22] Ü. Parts, V. M. H. Ruutu, J. H. Koivuniemi, M. Krusius, E. V. Thuneberg, and G. E. Volovik, Physica B **210**, 311 (1995).

[23] A. J. Leggett, Ann. Phys. (USA) **85**, 11 (1974).

[24] A. L. Fetter, in *Progress in Low Temperature Physics*, Vol. X, ed. D. F. Brewer (North-Holland, Amsterdam, 1986).

[25] E. Cheng, M. W. Cole, W. F. Saam, and J. Treiner, Phys. Rev. Lett. **67**, 1007 (1991); Phys. Rev. B **46**, 13967 (1992).

[26] P. J. Nacher and J. Dupont-Roc, Phys. Rev. Lett. **67**, 2966 (1991).

[27] H. Alles, A. V. Babkin, P. J. Hakonen, J. P. Ruutu, J. T. Salojärvi, and J. P. Saramäki, J. Low Temp. Phys. **102**, 21 (1996).

[28] K. W. Schwarz, Phys. Rev. B **31**, 5782 (1985).

[29] E. S. Sabisky and C. Anderson, Phys. Rev. A **7**, 790 (1973).

[30] P. Bhattacharyya, T.-L. Ho, and N. D. Mermin, Phys. Rev. Lett. **39**, 1290 (1977).

[31] Y. R. Lin-Liu, D. Vollhardt, and K. Maki, Phys. Rev. B **20**, 159 (1979).

[32] P. G. DeGennes and D. Rainer, Phys. Lett. **46A**, 429 (1974).

[33] A. L. Fetter, Phys. Rev. B **14**, 2801 (1976).

[34] E. V. Thuneberg, Physica B **210**, 311 (1995).

[35] D. Vollhardt and K. Maki, Phys. Rev. B **20**, 963 (1979); **23**, 1489(E) (1981).

[36] J. S. Korhonen, A. D. Gongadze, Z. Janú, Y. Kondo, M. Krusius, Yu. M. Mukharsky, and E. V. Thuneberg, Phys. Rev. Lett. **65**, 1211 (1990).

[37] A. J. Leggett and S. Takagi, Ann. Phys. (NY) **106**, 79 (1977).

[38] Yu. M. Bunkov, V. V. Dmitriev, A. V. Markelov, and Yu. M. Mukharskii, Phys. Rev. Lett. **65**, 867 (1990).

[39] J. S. Korhonen, Y. Kondo, M. Krusius, E. V. Thuneberg, and G. E. Volovik, Phys. Rev. **47**, 8868 (1993).

[40] V. B. Eltsov, T. W. B. Kibble, M. Krusius, V. M. H. Ruutu, and G. E. Volovik, Phys. Rev. Lett. **85**, 4739 (2000).